Proceedings of ASME Turbo Expo 2011
GT2011
June 6-10, 2011, Vancouver, British Columbia, Canada

GT2011-45236

EXPERIMENTAL INVESTIGATIONS OF CORNER STALL IN A LINEAR COMPRESSOR CASCADE

MA Wei *(1,2), **OTTAVY Xavier** (1), **LU Lipeng** (2), **LEBOEUF Francis** (1), **GAO Feng** (1,2)

(1) Laboratoire de Mécanique des Fluides et d'Acoustique, Ecole Centrale de Lyon, 69134, France
(2) Beijing University of Aeronautics and Astronautics, 100191 Beijing, China

ABSTRACT

In order to gain a better knowledge of the mechanisms of corner stall and to calibrate computational-fluid-dynamics (CFD) tools including both Reynolds-averaged Navier-stokes and large eddy simulation, a detailed and accurate experiment of three-dimensional flow field through a linear compressor cascade has been set up. Experimental data were acquired for a Reynolds number of 3.82×10^5 *based on blade chord and inlet flow conditions.*

First, inlet flow conditions were surveyed by hot-wire anemometry in boundary layers.

Second, in order to investigate the effects of incidence, measurements then were acquired at five incidences from -2° to 6°. The results included the outlet flow variables of the cascade, measured by a five-hole pressure probe, and static pressures on both blade and endwall surfaces, measured by pressure taps.

Third, the flow field details were measured at an incidence angle of 4°. In this configuration the corner stall region was large enough to be investigated, and without two-dimensional (2D) separation at mid-span on the blade suction side near the trailing edge. The velocity field was then measured by 2D Particle Image Velocimetry in cross-sections parallel to the endwall. And the velocity field in the vicinity of the blade suction side was measured with 2D Laser Dropper Anemometry.

In order to test the performance of CFD and also to validate the experimental results, a series of numerical simulations were carried out and compared with the experimental results.

We thus obtained a set of detailed measurements which constitute an original and complete data base and in good agreement with the published experimental results in literature. These data were also compared with CFD results and showed that the improvements needed in turbulence modeling in order to accurately simulate the three-dimensional separation configuration of corner stall.

NOMENCLATURE

c_a axial chord
C_p coefficient of static pressure
d diameter of hot-wire probe
δ^* displacement thickness
δ_3 energy thickness
H shape factor
i incidence
l active length of hot-wire probe
s^* position of LDA measuring line
Re_c Reynolds number based on blade chord
Re_θ Reynolds number based on momentum thickness
n the distance to the blade surface
ν kinematic turbulence viscosity
θ momentum thickness
Tu turbulence intensity
U_∞ inlet velocity
u' fluctuation velocity
u_τ friction velocity
ω total pressure loss coefficient

*wei.ma@ec-lyon.fr

Copyright © 2011 by ASME

ω^* pitchwise-mass-averaged total pressure loss coefficient
$\omega^{'}$ mass-averaged total pressure loss coefficient

1 INTRODUCTION

The juncture of the endwall and blade corner region is one of the high-loss regions in compressors [1]. The three-dimensional separation in this region, also referred as corner stall or corner separation, is an inherent flow feature in compressors. Alleviating corner stall is the key to improved efficiency and stability of compressor [2]. A number of studies have been carried out to investigate the impacts, the flow topology, the influencing factors, as well as global consequence of corner stall [3–8]. Though some of the deleterious consequences of corner stall can be identified, an effective control of these effects is very difficult to achieve. This is because of the fact that the nature and characteristics of these separations are still neither clearly understood, nor the mechanisms and factors that influence their growth and size fully quantified [7]. Corner stall is caused mainly by the strong streamwise pressure gradient, the presence of secondary flow and the merging of the wall and blade boundary layers; it is beyond the scope of the theories of boundary layer and secondary flow. Computational fluid dynamics (CFD) is a powerful tool to simulate corner stall flows, but only the overall pattern of corner stall can be captured while flow details are most of the time not well computed [9]. Today large eddy simulation is one of the more promising models of numerical simulation of turbulence [10, 11], but it still needs to be calibrated for turbomachinery applications.

In order to gain a better knowledge of the mechanisms of corner stall and to calibrate CFD tools including both Reynolds-averaged Navier-Stokes (RANS) and large eddy simulation (LES), a detailed and accurate experiment of three-dimensional flow field through a linear compressor cascade has been set up in the Laboratoire de Mécanique des Fluides et d'Acoustique (LMFA) at Ecole Centrale de Lyon. Experimental data were acquired for a Reynolds number of 3.82×10^5 based on blade chord and inlet flow conditions. Measurements have been achieved using hot-wire anemometry, pressure taps on blade and endwall, five-hole pressure probe, two-dimensional (2D) particle image velocimetry (PIV), and 2D laser Doppler anemometry (LDA).

In order to test the performance of CFD and also to validate the experimental results, a series of numerical simulations were carried out and compared with experimental results.

2 APPARATUS AND INSTRUMENTATION

In this section, we will introduce the facilities arrangement and uncertainties of each experimental result. All the data were acquired and recorded and all the device were controlled using a PC with routines of NI LabVIEW^{TM}.

2.1 Wind Tunnel and Cascade

The investigation was carried out with a low speed cascade wind tunnel. The facility is powered by a 60KW centrifugal blower and the test section is a rectangular duct with a cross section which is 900mm high by 370mm wide. The cascade consists of 13 NACA65-009 blades, as depicted in Fig. 1. The notation used in describing this subsonic compressor cascade is shown in Fig. 2. The cascade parameters are summarized in Table 1. In our experiment, inflow velocity was $U_\infty = 40.0 \pm 0.3 m/s$, corresponding to a chord Reynolds number $\mathrm{Re}_c = U_\infty c/\nu = 3.82\times10^5 \pm 2866$ ($\nu = 1.57\times10^{-5} m^2/s$). The difference in the inlet flow velocity was less than 0.5% in the pitchwise direction at the middle of the wind tunnel, i.e. the region where the flow was investigated.

In order to ensure and fix the location of the boundary layer transition which has large consequences on the corner zone separation, 3.0mm widthwise sand paper strips have been stuck at 6.0mm from the leading edge of both suction side and pressure side of all the blades. The transition simulation is particularly complex to be carried out with CFD, thus the authors wanted to remove this difficulty and focus the study only in the corner stall region.

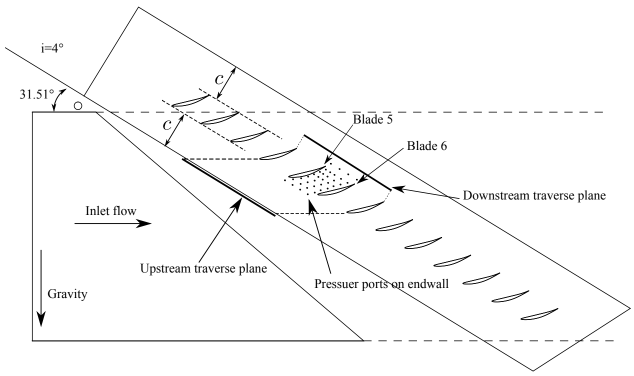

FIGURE 1. Plan-view of the wind tunnel test section

2.2 Temperature and Pressure Measurement System

A thermocouple type K was used to measure temperature, connected with the National Instruments thermocouple input module (NI-9211), then output voltage was recorded by the National Instruments data acquisition card (NI-cDAQ-9172). The uncertainty of the temperature was $\pm1^\circ$.

Forty pressure taps have been positioned at 34.2% span on a blade (the blade 5 in Fig. 1) located in the middle of the test section. The span of this instrumented blade was $1.58h$, where h is the blade span of the cascade. Twenty five taps were located on the suction side while the other fifteen taps were located on

Copyright © 2011 by ASME

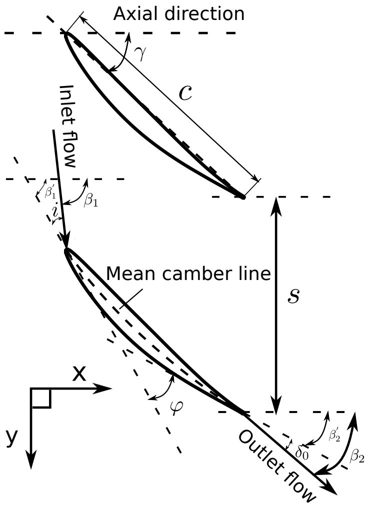

FIGURE 2. Notation for cascade

TABLE 1. Geometric parameters of the cascade

Symbol	Parameter	Magnitude
c	chord	150.0 mm
φ	camber angle	23.22°
γ	stagger angle	42.70°
s	pitch/spacing	134.0 mm
σ	solidity	1.12
h	blade span	370.0 mm
AR	aspect ratio	2.47
i	incidence angle	-5° $\sim$ 7°
i^*	optimum incidence	0.18°
β_1'	design upstream flow angle	54.31°
β_1	actual upstream flow angle	$=\beta_1'+i+i^*$
β_2'	design downstream flow angle	31.09°
β_2	actual downstream flow angle	$=\beta_2'+\delta^0$
δ^0	flow deviation angle	
θ	flow turning angle	$=\beta_1-\beta_2$

the pressure side. The pressure taps on the blade were made by 1.6*mm* diameter alloy steel tubing embedded into the blade surface, with a port of 0.8*mm* opening to the flow. This instrumented blade can slide in the spanwise direction through two slots (having the blade profile) on each side of the endwall. Leakage was prevented by o-rings around the profile. Static pressure can then be measured at any arbitrary section in the spanwise direction.

In order to measure the static pressure on the endwall, thirty five pressure taps have also been set up on the endwall. The pressure taps on the blade were made by 4.0*mm* diameter alloy steel tubing embedded into the endwall surface, with a port of 0.8*mm* opening to the flow.

A five-hole pressure probe was used to measure the outlet flow.

The pressure taps on the blade and the endwall were connected to a scanivalve. Using plastic tubes, both the Pitot-static probe and the scanivalve were attached to electronic pressure transducers (VALIDYNE™Model DP45-XX, the number XX indicating the pressure range). Then the pressures were monitored using Carrier Demodulators, which have an output voltage range of $\pm 10V$. Transducer output voltage was recorded by National Instruments data acquisition card (NI-cDAQ-9172) through a National Instruments C Series module (NI-9205).

The relative uncertainty of the pressure measurements both on the blade and the endwall was about 1% in static pressure coefficient values. The relative uncertainty of the downstream pressure measurements was about 2% in total pressure coefficient values.

2.3 Hot-Wire Anemometry

The inlet boundary layer was measured by a one-dimensional hot-wire system. Boundary layer probes Dantec 55P05 were used. The sensors were operated by a Dantec 90C10 constant temperature anemometer unit in Dantec Streamline. Square wave test was used to optimize the bandwidth of the combined sensor/anemometer circuit. The bandwidth of the probe/anemometer system (or cut-off frequency) of one-dimension hotwire in our experiment was about 60 kHz. According to the Nyquist sampling criteria, a sampling rate of at least 120 kHz was needed. The acquisition frequency was set as 200 kHz. The number of samples obtained was one million.

The probe stem was roughly aligned with the flow and placed at about 140 mm upstream of the 6.0-mm-diam horizontal rod used for support. The rod was held by a computer-controlled traverse gear located outside of the test section and passed through a 10.0-mm-wide slot in the endwall of the cascade. Plastic sheet and magnet were used to minimize the amount of air leaking through the slot. To reduce the impact of the gap in traverse gear on the uncertainty in traverse positions, traverse gear to the measuring points were in one direction. The contact (zero-distance) between the hot wire probe and endwall was achieved by using an electric circuit [12]. The uncertainty in traverse positions was 0.05 mm. Hot-wire signals were corrected for ambient temperature, and probes were calibrated by a fourth-order polynomial to correlate the wire output voltages with cooling velocities.

The uncertainty of mean streamwise velocity U was $1\%U_\infty$.

 Copyright © 2011 by ASME

The relative uncertainty of root-mean-square of fluctuation velocities u'_{rms} were and 3%.

2.4 2D PIV

By measuring the displacement of particles in a time interval, the velocity of the particles was calculated and assumed to be the local velocity of the flow field. A CCD camera with resolution of 1280×1024 pixels was used. The light source was a dual cavity Nd:YAG laser, developed by Quontel Incorporation, the maximum illumination energy was 120mJ/pulse. The commercial Lavision program DAVIS was used for acquisition and post processing. The frequency of image acquisition was 4 Hz, and the time delay between two frames was 10 μs. The size of the imaged region was $100mm \times 80mm$. A sequence of 2000 pairs of images was acquired at each operation condition. Here we only present the time-averaged vorticity. The relative uncertainty of the magnitude to the mean velocity was less than 3%. The uncertainty of the flow angle was less than 2°.

2.5 2D LDA

LDA is a single point optical technique for measuring the direction and speed of fluid. By measuring the Doppler frequency-shift of the light scattered by tracer particles, one is able to calculate the velocity of the tracer particle and thus the flow velocity of the fluid. In our experiment, equipment used include Spectra-Physics Stabilite 2017 Laser beam, Dantec FiberFlow 60×41 transmitter, Dantec FiberFlow 60×24 manipulator, Dantec FiberFlow 60×61 2D probe, and Dantec BAS-F80 signal processor. The commercial Dantec Dynamics BSA Flow Software for LDA version 4.11.00 was used for acquisition and post processing. The response of the photo detector was used to find the point where the distance from wall was zero. The measurement volume was on the wall when the anode current of the photo detector was maximum. The shortest distance between measuring point and blade surface was about 0.2*mm*. Bragg shifting was employed, so the flow direction and measure 0 velocity can be distinguished by the LDA system. The sample number of the measuring points near the endwall ($n \leqslant 0.6mm$) was 200,000, and the corresponding relative uncertainty of the magnitude of mean velocity was less than 2%, the uncertainty of the flow angle was less than 2°. The sample number of the measuring points far from the endwall ($n > 0.6mm$) was 1,000,000, and the corresponding relative uncertainty of the magnitude of mean velocity was less than 0.5%, the uncertainty of the flow angle was less than 0.5°.

2.6 Experiment and CFD Compatibilities

Cascade is a simplified model of the flow field in compressor. It is very difficult to evaluate the reliability of the experimental set-up and its inlet conditions. For example, it is very difficult to guarantee the uniformity of the inlet flow condition because of the geometry of the cascade. Current RANS solvers with modern turbulence model are known to be able to simulate accurately some parameters of the flow field in a compressor cascade, particularly in the mid-span of the cascade where the flow field is attached and can be considered as quasi-two-dimensional with a weak influence of the blockage induced by the corner stall. Static pressure distribution on the blade is one of these parameters.

So the experimental/numerical comparison of the static pressure distribution on the blade at mid-span can be used to validate the reliability of the experimental set-up, especially concerning the incident angle which is one of the most difficult parameter to adjust. At the same time, the comparison of the static pressure distribution on the blade near the endwall (in the separation) can reflect the necessity of the experiment.

Numerical calculation method The commercial computational fluid dynamics software package FLUENT was used. The convergence required that the scaled residuals decrease to 1.0E-11 for all equations.

The computational grid used in the current investigation was generated by AutoGrid 5, a commercial software package. The multi-block method was used to ensure the grid quality, as well as the matching periodicity strategy. Three girds with different grid densities were tested to check the grid independence of the solutions. Finally the grid with 976,640 cells was chosen for this numerical work. The first cell width from the surface of the blade and endwall was set to $n^+ = nu_\tau/\nu \sim 1$, where n is the distance from the cell to the surface of blade and endwall, u_τ is the local friction velocity. The maximum expansion ratio and the minimum skewness angle were set to 2.4 and 44°, respectively. To be able to compare these results with the experimental results, the inlet and the exit of the computation domain were placed at 2.16 axial chords upstream from leading edge and 1.36 axial chords downstream from trailing edge of the blade, respectively.

In the computation the flow was assumed to be steady and fully turbulent. The inlet velocity profile was obtained from the hotwire in the experiment and the incidence angle were specified for the inlet boundary, whereas the static pressure was used for the outlet boundary. The turbulent viscosity of 0.8% was specified for inlet boundary while the turbulent viscosity ratio 10 was specified for outlet boundary. Furthermore, nonslip and adiabatic conditions were adopted for all of the solid walls. Periodic conditions were imposed along the pitchwise boundaries.

A second-order upwind scheme and the central-differencing scheme were used for the convection terms and the viscous terms of each governing equation, respectively, to minimize the numerical diffusion. The pressure-velocity coupling was handled by the SIMPLE algorithm. Two turbulence models, the Spalart-Allmaras model and the standard k-ε model, were employed in the computational study and compared with the results of the experiment.

Copyright © 2011 by ASME

Compared with experiment Comparisons of static pressure coefficients on the blade between experimental and CFD results are shown in Fig. 3. At mid-span, the CFD results reproduce accurately the pressure distribution on the both sides of the blade. It obviously means that this experimental set-up and its generating conditions are reliable. In the vicinity of the endwall this CFD fails to reproduce the pressure distribution of the three-dimensional separations. This is the primary motivation for such experiments to be carried out in order to provide a calibration database for advanced CFD.

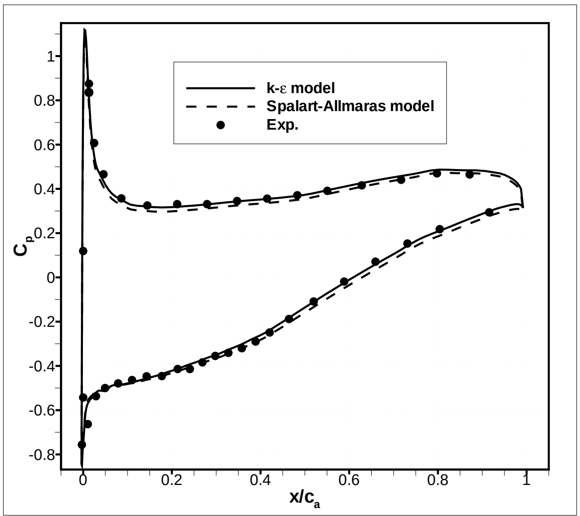

(a) $z/h = 185mm/370mm = 50.0\%$, mid-span

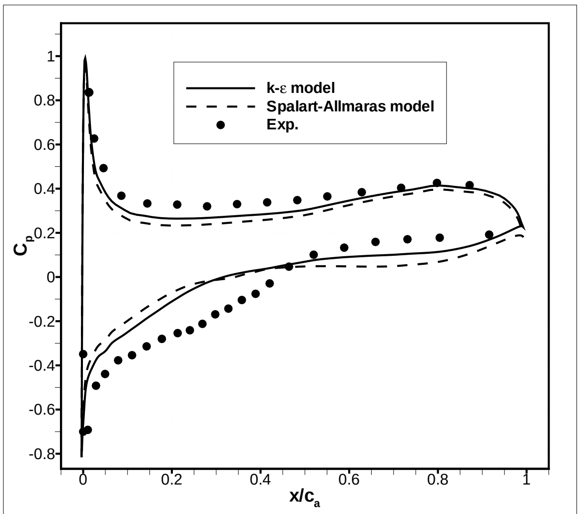

(b) $z/h = 20mm/370mm = 5.4\%$, near endwall

FIGURE 3. Comparison of pressure coefficient between experimental and numerical results, $i = 4°$, the uncertainty was 1% in experimental C_p values

3 EXPERIMENTAL RESULTS AND DISCUSSIONS
3.1 Inflow Conditions

TABLE 2. Positions of 1D hotwire measuring lines

NO.	L1	L2	L3	L4	L5
x	$-2.16c_a$	$-2.16c_a$	$-2.16c_a$	$-2.16c_a$	$-2.16c_a$
y^*	$-0.5s$	$0s$	$0.5s$	$1.0s$	$1.5s$
z	$0 \sim h/2$	$0 \sim h/2$	$0 \sim h/2$	$0 \sim h/2$	$0 \sim h/2$

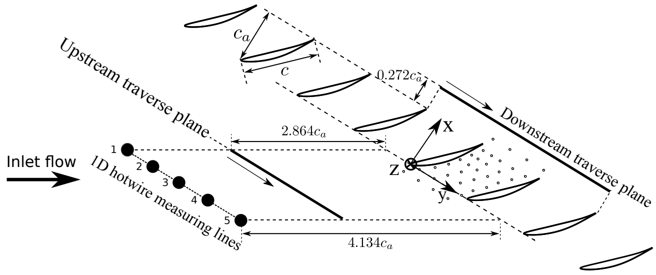

FIGURE 4. Illustration of 1D hotwire measuring lines

3.1.1 Boundary Layer Profile and Thickness
One-dimensional hot wires were used to measure the inlet flow velocity profile along five lines in spanwise direction (Fig. 4). The measuring lines were located at $5.2c_a$ from the leading edge of blade. Their coordinates are listed in Table 2, where c, s and h are chord, pitch and blade span, respectively, and y^* is the fraction of the cascade pitch, $y^* = 0$ corresponds to the position aligned with the leading edge of the blade 5. Three hotwire probes were used (P0, P1, P2), while the active length of the hot-wire l was $1.25mm$, $0.82mm$ and $1.00mm$, respectively, and the diameter d of the probe was $5.0\mu m$, $4.0\mu m$, and $4.0\mu m$, respectively. To avoid the conduction errors, l/d of a hot wire were greater than 200.

Established turbulent boundary layer can be divided into three zones: the viscous sublayer ($z^+ < 5$) where $u^+ = z^+$, the buffer layer ($5 < z^+ < 50$) and the logarithmic layer ($50 < z^+ < 600$) with the logarithmic law of the wall, or 'log law', given by $u^+ = 1/\kappa(\ln z^+) + B$. We derived the wall shear stress τ_w from a best fit to the log law between $z^+ = 50$ and $z^+ = 600$, using the Coles log law constants: $\kappa = 0.41$ and $B = 5.21$, the friction velocity is then $u_\tau = \sqrt{\tau_w/\rho}$.

Experimental results of the inlet flow velocity profiles are shown in Fig. 5(a,b), in which the red curve is from the Van Driest formula [13]. According to Fig. 5(b), the inlet flow boundary

Copyright © 2011 by ASME

TABLE 3. Parameters of inlet boundary layer used hot-wire anemometry

NO.	δ_{99} (mm)	δ^* (mm)	θ (mm)	δ_3 (mm)	$H = \delta^*/\theta$	$\mathrm{Re}_\theta = \theta u_e/\nu$	u_τ (m/s)	τ_w (kg/ms^{-2})	$l^+ = lu_\tau/\nu$
L1-P0	30.1	3.7	2.9	5.2	1.29	7323	1.46	2.494	116
L2-P0	29.1	3.8	2.9	5.3	1.28	7495	1.46	2.494	116
L3-P0	30.1	4.0	3.1	5.6	1.29	7918	1.46	2.494	116
L3-P2	30.1	4.0	3.1	5.8	1.29	7918	1.44	2.426	92
L4-P0	32.1	4.5	3.5	6.3	1.28	8888	1.46	2.494	116
L4-P1	31.1	4.8	3.7	6.7	1.30	9489	1.43	2.393	75
L5-P1	30.1	4.1	3.2	5.7	1.28	8051	1.45	2.494	76

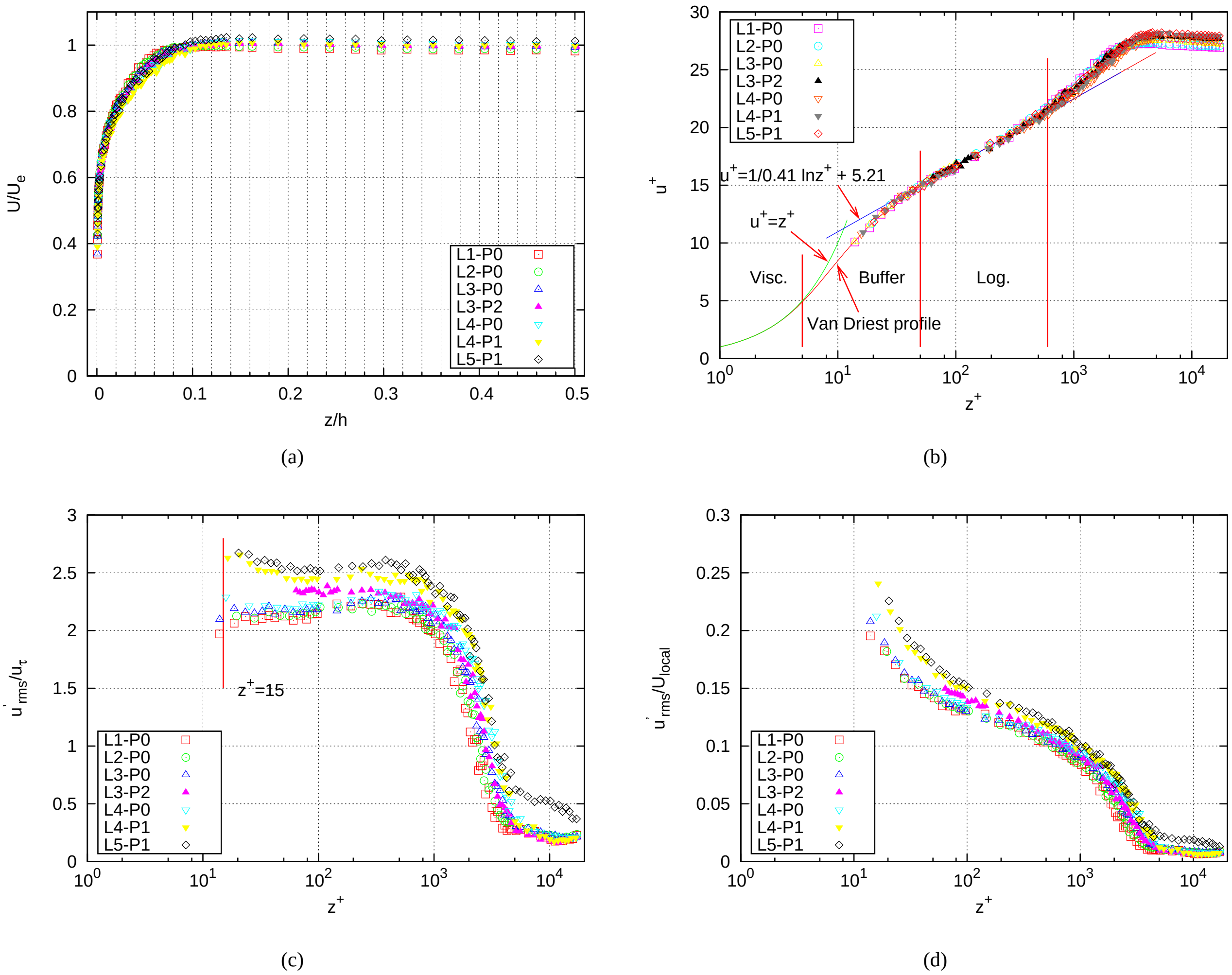

FIGURE 5. Experimental results of inlet boundary layer using hot-wire anemometry

Copyright © 2011 by ASME

layer is fully turbulent and the first measuring points are in the buffer layer. The closest distance of the wire to the endwall is $z^+ = 14$, outside of $z^+ < 4$ where exists a considerable effect of the wall confirmed by Durst et al [14]. Note that the inlet flow is not totally uniform: the velocity at mid-span increases a bit in the z direction, because of the influence of the test rig skewness. The difference (< 1.5%) however remains very small.

Based on the velocity profile, various boundary-layer parameters are calculated and listed in Table 3, where $\mathrm{Re}_\theta = \theta U_\infty/\nu$, $\nu = 1.57\times10^{-5} m^2/s$. In this table, "L1-P2" is a label for the results of line "L1" defined in Table 2 using the number "2" hot-wire probe. The boundary-layer thickness, δ, is defined here as the distance from the wall to the point where $U(z) = 0.99U_\infty$. δ^*, θ and δ_3 are displacement thickness, momentum thickness and energy thickness, respectively. In our experiment, $7300 < \mathrm{Re}_\theta < 9500$, and the shape factor is $H = \delta^*/\theta \approx 1.3$, smaller than the value in Ref. [15] with the same Re_θ. This is because of the existence of a favorable pressure gradient in our cascade in the upstream region [15, 16].

3.1.2 Streamwise Normal Stress

Profiles of u'_{rms}/u_τ which resolve the near-wall behavior, show a peak very near the wall, but the magnitude and location are still in doubt [17]. Fernholz [16] considered the maximum value of $u'_{rms}/u_\tau \sim 2.7$, and its position, $z^+ \sim 15$, and according to experimental results, they suggested that the peak of u'_{rms}/u_τ has a slightly rising trend with falling l^+ and with rising Re_θ ($l^+ = lu_\tau/\nu$ being a dimensionless characteristic of the hot-wire length scale). Since a hot wire measures the average heat transfer rate over its length, it will weaken the measured velocity fluctuation if that fluctuation occurs over a length-scale smaller than the length of the hot wire. If it is assumed that the characteristic eddy size is taken by the distance to the wall, and that a non-negligible fraction of the turbulent kinetic energy is carried by eddies with this characteristic size, then a hot wire will significantly weaken the measured turbulence intensity when it is positioned closed to the wall.

The experimental profiles of u'_{rms}/u_τ and local turbulence intensity $Tu_{local} = u'_{rms}/U_{local}$ are shown in Fig. 5(c-d). Inside the turbulent boundary layer, there are obvious differences between the experimental results obtained with the different hot-wire probes. According to the analysis above, the $(u'_{rms}/u_\tau)_{max}$ reaches 2.3 with the P0 and 2.7 with the P1 mainly because of the difference in l^+ of the used hot-wire probes. The little discrepancies between the boundary layer characteristics using the same probe is because that Re_θ changes by a little bit at the locations that were investigated .

Outside of the boundary layer, the differences between the boundary layer profiles are mainly due to the non-uniformity of the inlet flow. The local turbulence intensity $Tu_{local} \approx 0.8\%$ for most of the inlet flow, from line 1 to line4, except $Tu_{local} \approx 1.3\%$ for line 5.

3.2 Effect of Incidence

Incidence is one of the most important influencing factors of corner stall. To assess the effects of the incidence on the flow behavior and the overall performance of the cascade, pressure measurements have been carried out for incidences from -2° to 6°.

Conventional dimensionless form of local static pressure coefficient C_p and local total pressure loss coefficient ω are given as $C_p = (p - p_\infty)/(p_{t\infty} - p_\infty)$, $\omega = (p_{t\infty} - p_t)/(p_{t\infty} - p_\infty)$, Where $p_{t\infty}$ and p_∞ are the reference inlet total and static pressure, while p_t and p are the total and static pressure at the desired point, respectively.

3.2.1 Surface Static Pressure on Blade

The spanwise distribution and the contours of surface static pressure on the blade at $i = 4^\circ$ are shown in Fig. 6. Pressure is nearly constant on the blade pressure side in the spanwise direction except in the region near the endwall at leading edge, because of the boundary layer of endwall. The contours on the suction side clearly indicate the low-pressure regions from endwall to $z/h = 20\%$ due to corner stall from the leading edge to the trailing edge.

The comparisons of surface static pressure on the blade at different incidences at two sections are shown in Fig. 7(a,b), where the first one is at mid-span ($z/h = 50\%$), the other one is near the endwall and in the region of corner stall ($z/h = 5.4\%$). Fig. 7(c,d) shows the pressure force in x and y directions, defined as $F_x = \oint C_p\vec{n}\cdot\vec{i}dl/c_a$, $F_y = \oint C_p\vec{n}\cdot\vec{j}dl/c_a$, where $\vec{n}$, $\vec{i}$ and $\vec{j}$ are unit normal vector of blade surface and x and y axes, respectively.

The pressure on the pressure side increases with incidence. The pressure distribution on suction side can be divided into two parts. In the front part ($0 < x/c_a < 20\%$) near the leading edge, the static pressure at first accelerates and then decelerates owing to the flow turning around the leading edge. This indicates that the velocity at first decelerates and then accelerates. In this part the static pressure decreases with increasing incidence. In the latter part ($20\% < x/c_a < 100\%$), the static pressure at first decelerates and then reaches a constant values. This indicates that flow at first decelerates and then separates. In this part the static pressure increases and the extent of separation increases with increasing incidence.

Similar trends have been observed for the pressure at $z/h = 5.4\%$ compared with mid-span. Some specific phenomena related to flow separation are observed. The pressure evolutions reach constant values after a specific axial position, even at negative incidence, indicating the areas of flow separation. The position of separation moves upstream when the incidence increases. From Fig. 7(b), the separation occurs around $x/c_a = 0.6$ for instance at $i = 4^\circ$. Considering again Fig. 6(b), a strong inclination of the Cp isolines for $z/h < 0.3$ is also observed; this is the direct

Copyright © 2011 by ASME

consequence of the blockage effect induced by the corner separation which induces curvature in the flow up to the leading edge (see [18]).

The blade pressure force F_x and F_y increases along spanwise direction for all incidence are observed, and its increase also when incidence grows, except when $i = 6^\circ$ or $z/h < 0.2$. We can infer that there are stronger separations at $i = 6^\circ$ than at other incidences, and this will be confirmed by the experimental total pressure losses in the exit plane as discussed in section 3.2.3.

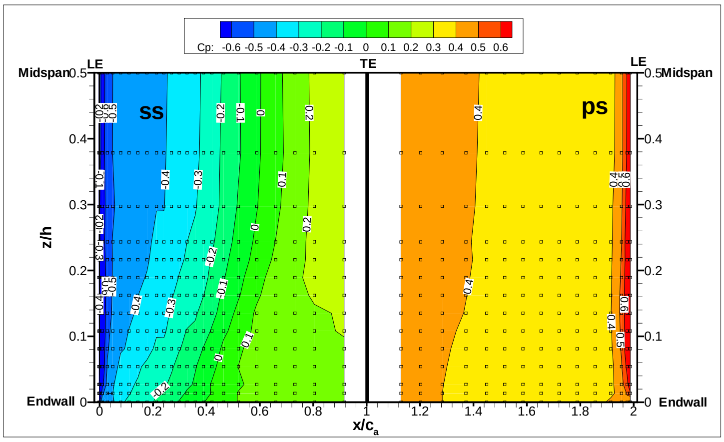

FIGURE 6. Contours of C_p on blade surface, $i = 4^\circ$, markers indicate the positions of measuring points

3.2.2 Surface Static Pressure on Endwall

The pressure coefficients on the endwall at different incidences are shown in Fig. 8. The extent of the region where the flow accelerates from the leading edge narrows with incidence, which is consistent with the experimental results of surface static pressure on blade discussed in section 3.2.1. With increasing incidence, the location of separation point moves forward to leading edge and the extent of the corner separation expands. In this range of incidence with increasing incidence, the ratio of outlet pressure to inlet pressure increases in the passage near suction side on the endwall.

3.2.3 Total Pressure Losses of Outlet Flow

The contours of the exit total pressure loss coefficient at the cascade exit plane at 36.3% axial chord downstream from trailing edge at different incidences are shown in Fig. 9. To quantify the global effects of the total pressure loss at the cascade outlet, two parameters are used (Fig. 10), which are the pitchwise-mass-averaged total pressure loss coefficient ω^* and the mass-averaged total pressure loss coefficient ω' defined as

$$\omega^*(z) = \frac{\int_0^s \omega(y,z) u_x(y,z) dy}{\int_0^s u_x(y,z) dy}$$

$$\omega' = \frac{\int_0^s \int_0^{h/2} \omega(y,z) u_x(y,z) dydz}{\int_0^s \int_0^{h/2} u_x(y,z) dydz}$$

where u_x is the axial velocity of outlet flow. ω^* is the function of spanwise distance from the given plane, while ω' just depends on the given plane.

At a certain incidence, the losses increase in the spanwise direction from mid-span to endwall. As mentioned before, the losses at mid-span due to quasi-two-dimensional separation increase with incidence, which is also observed clearly by the extent of loss region at different incidences in Fig. 9. From the contours in Fig. 9, we can come to the conclusion that the maximum losses as well as the extent of losses in the corner increase with incidence, and this is also confirmed by the value of ω^* and ω' at different incidences.

3.3 Detailed Experiment at $i = 4^\circ$

Oil visualization results (Fig. 11) were used to qualitatively indicate the global view of corner stall on both suction side and endwall. There were two obvious vortices, one was on suction side and the other one was on the endwall. Then the flow field details were measured at an incidence angle of 4°. Because in this configuration the corner stall region was large enough to be investigated, and without 2D separation at mid-span on suction side near the trailing edge. In cross-sections parallel to the endwall, the velocity field was then measured by 2D PIV and the velocity field in the vicinity of the blade suction side was measured by 2D LDA.

3.3.1 Ensemble Averaged Vorticity

The measuring plane was normal to the spanwise direction. According to the position of the laser and the camera shot size which guarantees enough spatial resolution, 14 sections along spanwise were measured and each section was divided into 6 zones ($100mm \times 80mm$).

The multi-pass interrogation was used. The particle-image displacement was at first estimated by using a 64×64 pixels interrogation window, and then by a 32×32 pixels interrogation window with 50% overlap. As a result, the final velocity vector grid spatial resolution was about 1.25mm.

The spanwise vorticity ($\omega_z = \partial U_x/\partial y - \partial U_y/\partial x$) only in one zone which contains the main feature of the corner stall as well as streamlines at section $z/h = 20mm/370mm = 5.4\%$ are shown in Fig. 12. It's observed clearly that low speed flow accumulates at the corner from endwall to $z/h = 50mm/370mm = 13.5\%$. The flow separates in this section at $x/c_a = 0.45$ from suction side, then mixes with the mainstream flow in the downstream region.

Copyright © 2011 by ASME

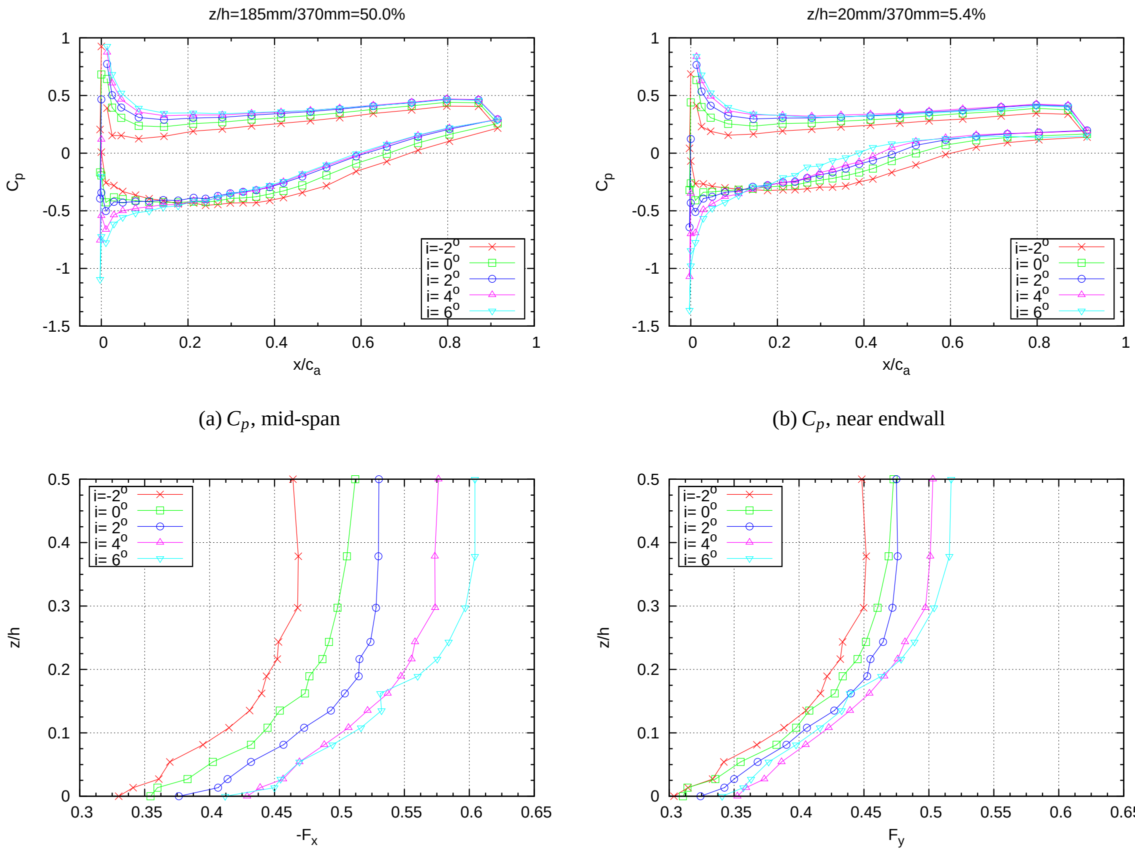

(a) C_p, mid-span

(b) C_p, near endwall

(c) Pressure force in x direction

(d) Pressure force in y direction

FIGURE 7. Comparisons of surface static pressure parameters on blade at different incidences

3.3.2 Velocity Profile in the Vicinity of Blade Suction Side

In our experiment, the velocity profiles on the suction side of the blade were measured by LDA, because LDA can measure the flow field much nearer to the blade surface than the PIV does, also LDA can measure reverse flow contrary to hot-wire anemometer.

The measuring section was perpendicular to the spanwise direction, so the velocity in axial direction u_x and the velocity in pitchwise direction u_z were measured. At every section, the measuring line was along the normal direction of the point located on blade suction side, as shown in Fig. 13. $\vec{n}$ and $\vec{s}$ are the unit vectors in the normal direction and the tangential direction of the point A. The measured velocity $\vec{u}$ can be decomposed into the velocity along the normal direction $\vec{u_n}$ and the velocity along the tangential direction $\vec{u_s}$. The velocity formula can be expressed as,

$$\vec{u} = \vec{u_x} + \vec{u_y} = \vec{u_n} + \vec{u_s} \tag{1}$$

In order to show the actual fluid displacements, $s^* = s/L$ is used to demarcate the positions along measuring line, where s is the arc length from the leading edge to the beginning point of measuring line A, and L is the arc length from the leading edge to the trailing edge.

The experimental results of LDA in the section at $z = 5mm$ are shown in Fig. 14, and the vector of mean velocity is shown in Fig. 15a. There is an obvious vortex in the passage of the cascade. According to the 2D separation criteria, in this section from the experimental results of mean velocity, the separation point is located at the position between $s^* = 0.35$ and $s^* = 0.40$. From the results of the standard deviation (in Fig. 14 (c,d)), we know that the turbulence intensity increases near the region of $s^* = 0.35 \sim 0.4$ and $n = 0mm \sim 10mm$, because of three- dimensional unsteady separation in this region.

The velocity flow fields obtained in plane $z = 5mm$ with the numerical simulation discussed above are also presented here, including the standard $k - \varepsilon$ (15b) and the Spalart-Allmaras model (15c). The separation point is located at $s^* = 0.30 \sim 0.35$ for the $k - \varepsilon$ model, while $s^* = 0.20 \sim 0.25$ for the Spalart-Allmaras

Copyright © 2011 by ASME

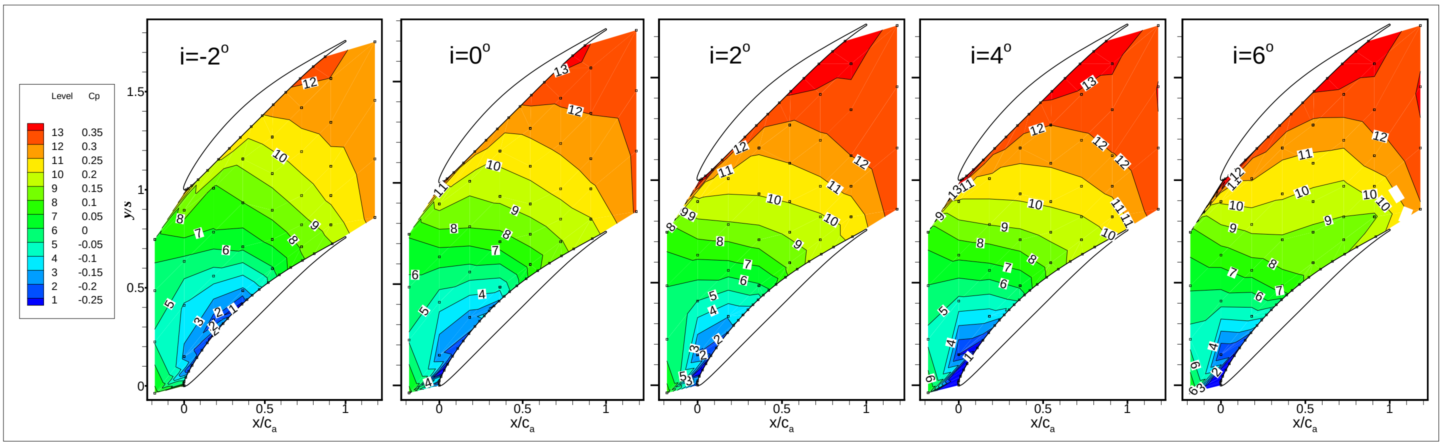

FIGURE 8. Static pressure coefficients on endwall at different incidences, markers indicate the positions of measuring points

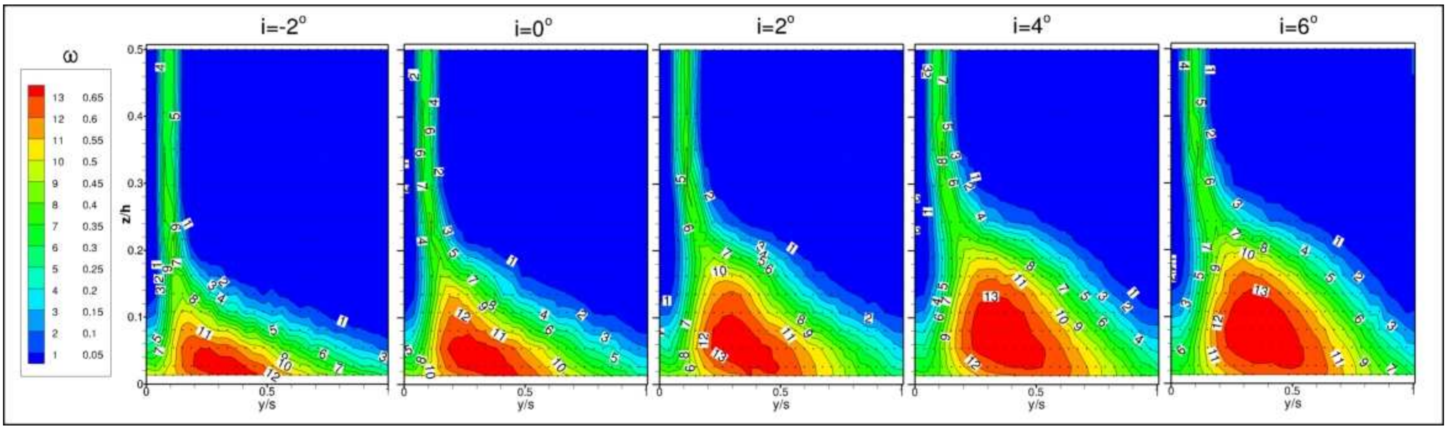

FIGURE 9. Contours of exit total pressure loss coefficient at 36.3% axial chord downstream from trailing edge at different incidences, markers indicate the positions of measuring points

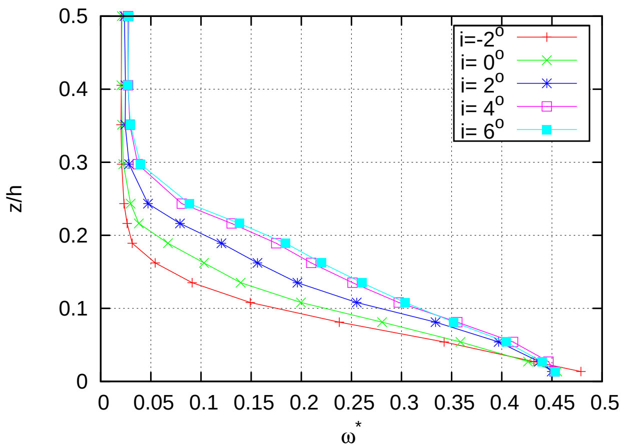

(a) Pitchwise-mass-averaged total pressure loss coefficient

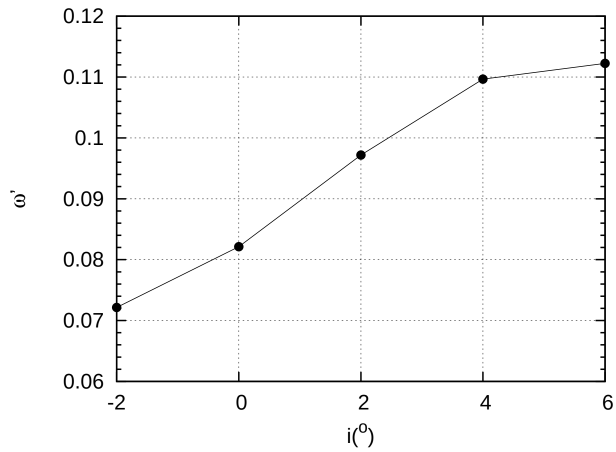

(b) Mass-averaged total pressure loss coefficient versus incidence

FIGURE 10. Two quantitative parameters at 36.3% axial chord downstream from trailing edge

Copyright © 2011 by ASME

FIGURE 11. Result of oil visualization, $i = 4^{\circ}$

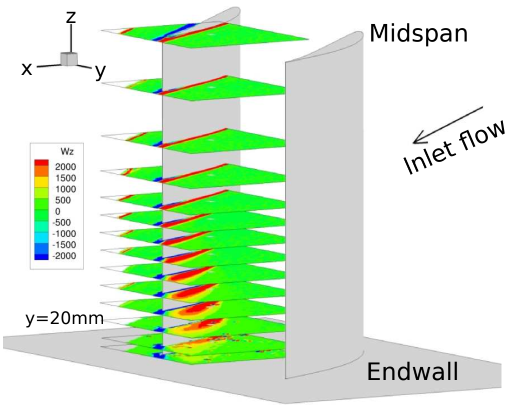

(a) In one zone

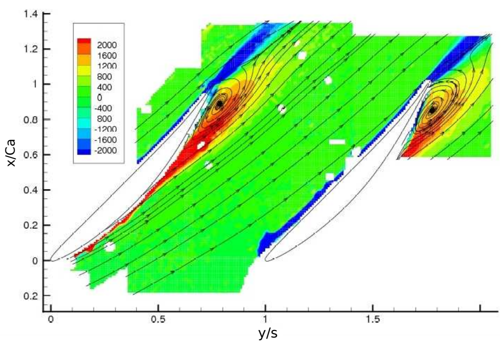

(b) z/h=20mm/370mm=5.4%

FIGURE 12. Vorticity in spanwise direction and streamlines of two-dimensional PIV results at, $i = 4^{\circ}$

model. The core of the passage vortex is located at $s^* = 0.70 \sim 0.80$ for $k-\varepsilon$ model, while $s^* = 0.70$ for the Spalart-Allmaras model. So the separation zone of Spalart-Allmaras model is a little ahead of the result of the $k-\varepsilon$ model.

In comparison with the experimental LDA result (Fig. 15a), shows that only the overall pattern of corner stall can be captured but not the details. For the position of separation point in

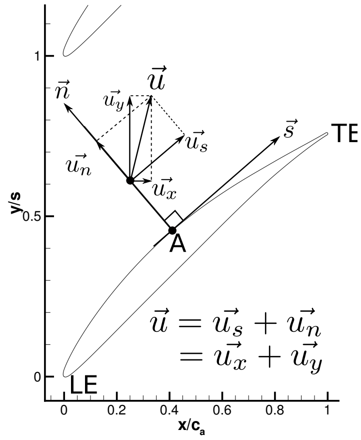

FIGURE 13. Diagram of velocity decomposition of 2D LDA results

the section near endwall, $k-\varepsilon$ model works better than Spalart-Allmaras model. The areas of separation zone of these two turbulence models are similar but smaller than the LDA result.

As discussed by Liu and Pletcher [19], the skewness of velocity fluctions represents the direction of energy transfer in physical space. Liu and Pletcher showed that in the streamwise direction, the turbulent energy is transferred forward in the viscous sublayer and the buffer sublayer, and backward at the remaining part; in the normal direction, the energy is produced in the buffer sublayer and transferred to both the viscous sublayer and the outer part. In our experiment, the mechanism is more complicated because of the effect of the corner flow. From Fig. 14(c), we can analyze the transport of turbulent energy in the streamwise direction. It is shown that when $s^* \leqslant 0.4$, most of the skewness values are negative, while when $s^* > 0.4$ they are positive in the range $n < 30mm$. Note that $s^* = 0.4$ is the boundary region of the corner flow. Fig. 14(c) therefore represents the backward energy transfer outside the corner flow and the forward transfer in the corner flow. From the skewness in the normal direction (not shown here), the negative values are located mainly in the range where $n < 40mm$ when $0.6 \leqslant s^* \leqslant 0.7$, and remains positive in most of the other regions. From these results we can approximately draw a sketch of the transport of turbulent energy in the plane of $z = 5.0mm$ as shown in Fig. 16.

We also plot the flatness of the velocity fluctuations in Fig. 14(d) to show the corresponding non-Gaussian properties. The value $Fl = 4$ corresponds to a Gaussian distribution. In the region where $n > 20mm$, the value of flatness is around 3.0, and when n is smaller the value obviously depends on other parameters. These results could be compared with numerical simulations in the future.

Copyright © 2011 by ASME

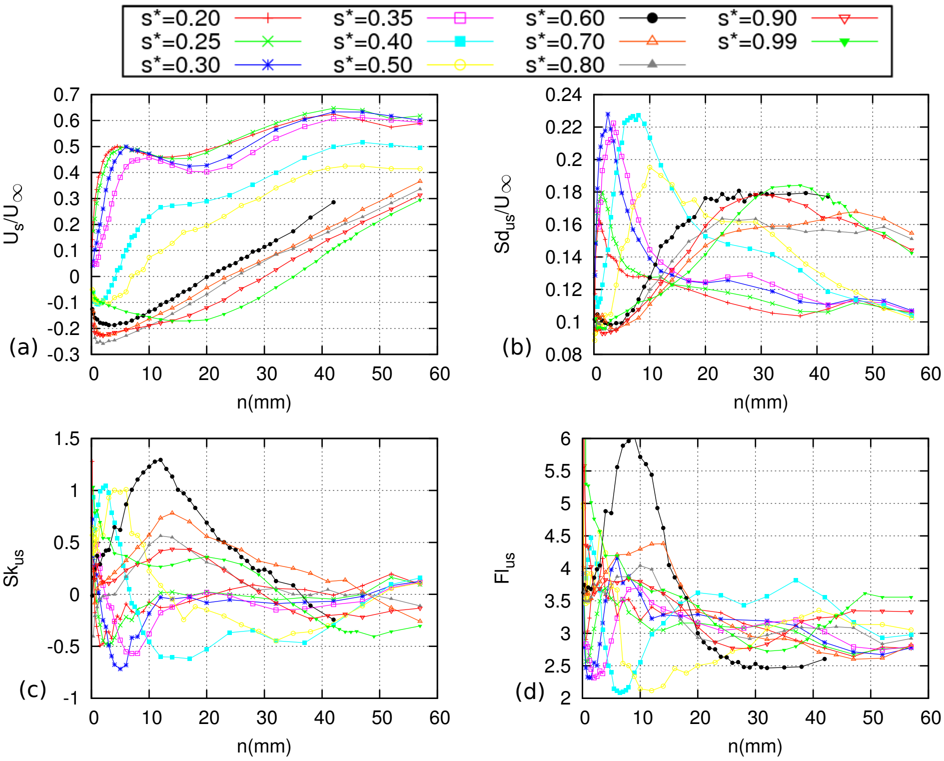

FIGURE 14. LDA results, $z/h = 5mm/370mm = 5.4\%$, near endwall, $i = 4^\circ$, (a) normalized mean velocity in tangential direction, (b) normalized standard deviation of $u_s^{'}$, (c) skewness of $u_s^{'}$, (d) flatness of $u_s^{'}$

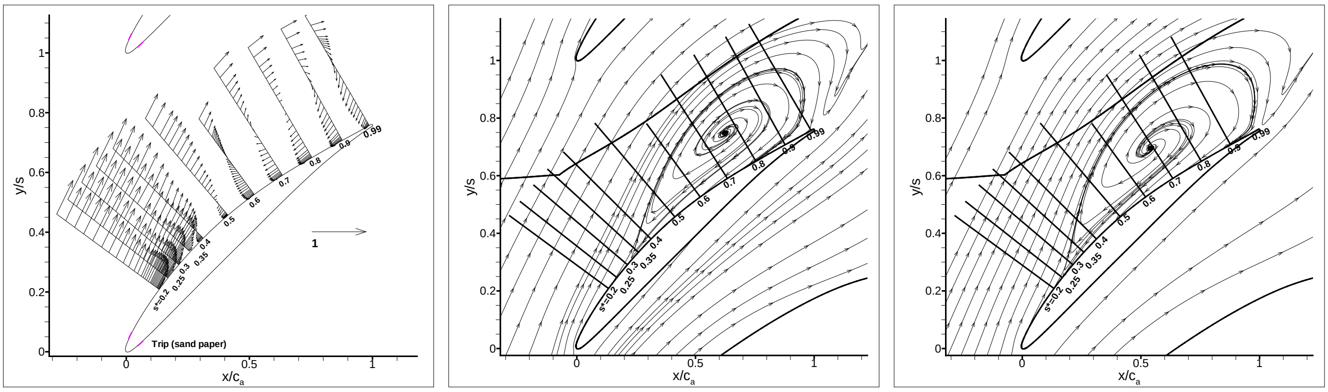

(a) Vector $\vec{u}/U_\infty$ of LDA experimental results

(b) $k-\varepsilon$ model

(c) Spalart-Allmaras model

FIGURE 15. LDA experimental results and numerical results, $z/h = 5mm/370mm = 5.4\%$, near endwall, $i = 4^\circ$

4 CONCLUSIONS

A linear compressor cascade experiment dedicated to the studies on the three-dimensional corner separation has been set up in LMFA at Ecole Centrale de Lyon. High attention has been taken in order to have some uniform and accurate inlet conditions.

A original and accurate data base has been built including detailed measurements of the inlet flow boundary layers, the surface static pressure on the blade and the endwall, the total pressure loss coefcient in outlet section at a series of incidences, the global features of the velocity flow field using 2D PIV, and the detailed measurements of the boundary layers that develop on the suction side of the blade in and out the separated zone using 2D LDA at a selected incidence. At mid-span of the blades where

Copyright © 2011 by ASME

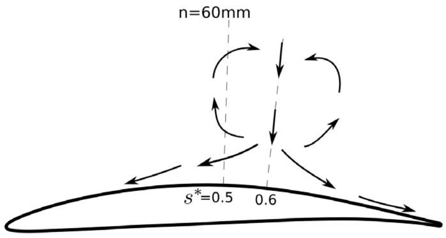

FIGURE 16. sketch of the transport of turbulent energy, $z/h = 5mm/370mm = 5.4\%$, near endwall

the flow is almost two-dimensional, the comparison with numerical RANS simulations shows a very good agreement of the pressure distributions, and proves the capability of this experimental setup to be numerically simulated. In the vicinity of the endwall, where the three dimensional separation occurs, the goal of this experiment is to provide a data based for advanced CFD, such as the improvement of the Spallart-Allmaras model (as proposed by Wang et al. [20]) and LES (as proposed by Boudet et al. [21]).

ACKNOWLEDGMENT

The authors would like to thank the reviewers for their comments that help improve the manuscript.

The authors wish to thank Sebastien Goguey, Gilbert Halter, Benoit Paoletti, and Pierre Laucher for their fine work in the experimental set-up.

The authors wish to express the sincere gratitude to the support from National Natural Science Foundation of China (Grant No. 50976010) and China 111 Project (Grant No. B08009). MA Wei and GAO Feng are supported by China Scholarship Council.

REFERENCES

[1] Wisler, D. C., 1985. "Loss reduction in axial flow compressors through low-speed model testing". *Journal of Turbomachinery,* ***107***(2), pp. 354–363.

[2] Cumpsty, N. A., and Greitzer, E. M., 2004. "Ideas and methods of turbomachinery aerodynamics: A historical view". *Journal of Propulsion and Power,* ***20***(1), pp. 15–26.

[3] Joslyn, H. D., and Dring, R. P., 1985. "Axial compressor stator aerodynamics". *Journal of Engineering for Gas Turbines and Power,* ***107***(2), pp. 485–493.

[4] Barankiewicz, W. S., and Hathaway, M. D., 1998. "Impact of variable-geometry stator hub leakage in a low speed axial compressor". *ASME 98-GT-194*.

[5] Schulz, H. D., and Gallus, H. E., 1988. "Experimental investigations of the three-dimensional flows in an annular compressor cascade". *Journal of Turbomachinery,* ***110***(4), pp. 467–478.

[6] Schulz, H. D., Gallus, H. E., and Lakshminarayana, B., 1990. "Three-dimensional separated flow field in the endwall region of an annular compressor cascade in the presence of rotor-stator interaction: Part 1-quasi-steady flow field and comparison with steady-state data; part 2-unsteady flow and pressure field". *Journal of Turbomachinery,* ***112***(4), pp. 669–678, 679–688.

[7] Gbadebo, S. A., Cumpsty, N. A., and Hynes, T. P., 2005. "Three-dimensional separations in axial compressors". *Journal of Turbomachinery,* ***127***(2), pp. 331–339.

[8] Lei, V.-M., Spakovszky, Z. S., and Greitzer, E. m., 2008. "A criterion for axial compressor hub-corner stall". *Journal of Turbomachinery,* ***130***(3), p. 031006.

[9] Denton, J. D., 1997. "Lessons from rotor 3". *Journal of Thermal Science,* ***6***(1), pp. 1–13.

[10] Sagaut, P., 2001. *Large Eddy Simulation for Incompressible Flows: An Introduction*. Springer.

[11] Garnier, E., Adams, N., and Sagaut, P., 2009. *Large Eddy Simulation for Compressible Flows*. Springer.

[12] Ottavy, X., and Hodson, H., 2000. The effects of wake-passing unsteadiness in high loaded axial compressor blades design - case of a flat plate. Tech. rep., White Laboratory, Cambridge University.

[13] van Driest, E. R., 1956. "On turbulent flow near a wall". *Journal of the Aeronautical Sciences,* ***23***(11), pp. 1007–1011, 1036.

[14] Durst, F., Zanoun, E. S., and Pashtrapanska, M., 2001. "In situ calibration of hot wires close to highly heat-conducting walls". *Experiments in Fluids,* ***31***(1), pp. 103–110.

[15] Österlund, J. M., 1999. "Experimental studies of zero pressure-gradient turbulent boundary layer flow". PhD thesis, Royal Institute of Technology, Stockholm, Sweden.

[16] Fernholz, H. H., and Finley, P. J., 1996. "The incompressible zero-pressure-gradient turbulent boundary layer: an assessment of the data". *Progress in Aerospace Sciences,* ***32***(4), pp. 245–311.

[17] DeGraaff, D. B., and Eaton, J. K., 2000. "Reynolds-number scaling of the flat-plate turbulent boundary layer". *Journal of Fluid Mechanics,* ***422***, pp. 319–346.

[18] Bario, F., Leboeuf, F., and Papailiou, K. D., 1982. "Study of secondary flows in blade cascades of turbomachines". *Journal of Engineering for Power,* ***104***(2), pp. 497–509.

[19] Liu, K., and Pletche, R. H., 2008. "Anisotropy of a turbulent boundary layer". *Journal of Turbulence,* ***9***(18), pp. 1–18.

[20] Wang, D., Lu, L., and Li, Q., 2009. "Improvement on sa model for predicting corner separation based on turbulence transport nature". *AIAA 2009-4931*.

[21] Boudet, J., Caro, J., Shao, L., and Lévêque, E., 2007. "Numerical studies towards practical large-eddy simulation". *Journal of Thermal Science,* ***16***(4), pp. 328–336.

Copyright © 2011 by ASME